

Stochastic Simulations of Bed Topography Constrain Geothermal Heat Flow and Subglacial Drainage near Dome Fuji, East Antarctica

Calvin Shackleton¹, Kenichi Matsuoka¹, Geir Moholdt¹, Brice Van Liefferinge¹, and John Paden²

¹Norwegian Polar Institute

²University of Kansas

May 25, 2023

Abstract

Dome Fuji, inland East Antarctica is one of only few regions where 1.5-Ma old ice can be preserved for investigating the mid-Pleistocene Transition. We used stochastic simulation and various radar datasets to generate a bed topography ensemble with the continuous, realistic roughness necessary to assess basal conditions. Ensemble analysis reveals the magnitude and spatial distribution of topographic uncertainty, facilitating uncertainty-constrained assessments of subglacial drainage and topographic adjustments to geothermal heat flow. We find that topographic variability can lead to widespread local geothermal heat flow variations of $\pm 20\%$ the background value, which aggregate to raise the regional value and suggest previously underestimated distributions and rates of basal melting. We also find that survey profile spacing has an increasing influence on topographic uncertainty for rougher bed, deriving an empirical relationship that could guide future survey planning based on uncertainty tolerance.

Stochastic Simulations of Bed Topography Constrain Geothermal Heat Flow and Subglacial Drainage near Dome Fuji, East Antarctica

Calvin Shackleton^{1*}, Kenichi Matsuoka¹, Geir Moholdt¹, Brice Van Liefferinge¹, and John Paden²

¹*Norwegian Polar Institute, Fram Senteret, Tromsø, Norway, 9296*

²*Center for Remote Sensing of Ice Sheets, The University of Kansas, Lawrence, KS, USA, 66045*

Corresponding author: Calvin Shackleton (*calvin.shackleton@npolar.no)

Key Points:

- Stochastic simulations yield uncertainty-constrained analyses of subglacial drainage and topography-adjusted geothermal heat flow (GHF).
- Order-of-magnitude rougher bed than previous work shows widespread local GHF variability, impacting regional-mean and bed conditions.
- New empirical relationship derived to implement bed-elevation uncertainty into radar survey planning for varying bed roughness.

Abstract

Dome Fuji, inland East Antarctica is one of only few regions where 1.5-Ma old ice can be preserved for investigating the mid-Pleistocene Transition. We used stochastic simulation and various radar datasets to generate a bed topography ensemble with the continuous, realistic roughness necessary to assess basal conditions. Ensemble analysis reveals the magnitude and spatial distribution of topographic uncertainty, facilitating uncertainty-constrained assessments of subglacial drainage and topographic adjustments to geothermal heat flow. We find that topographic variability can lead to widespread local geothermal heat flow variations of $\pm 20\%$ the background value, which aggregate to raise the regional value and suggest previously underestimated distributions and rates of basal melting. We also find that survey profile spacing has an increasing influence on topographic uncertainty for rougher bed, deriving an empirical relationship that could guide future survey planning based on uncertainty tolerance.

Plain Language Summary

The landscape beneath ice sheets affects ice flow, melt and refreeze at the base, subglacial drainage of meltwater, and presence of very old ice near the base which can be used for climate reconstruction. Dome Fuji, inland East Antarctica is one of few candidate sites for drilling an ice core that covers a major climatic change around 1 million years ago. Using ice thickness measurements from airborne and ground-based radar surveys with 0.25 – 10 km spacings, we simulated values between measurements to produce 100 possible continuous grids of the landscape beneath Dome Fuji. For each result we estimate the impact of valleys and ridges on geothermal heat distribution and predict water flow directions and lakes that store basal meltwater beneath the ice sheet. Averaged results show where processes are most likely to occur while also indicating uncertainty. We find that landscape variability beneath the ice sheet could increase the distribution and rates of deep ice melting. The uncertainty analysis we applied could also be used to assist the planning of future surveys aiming to map the landscape beneath thick ice in this region and elsewhere in Antarctica and Greenland.

1 Introduction

Subglacial topography drives fundamental ice sheet processes yet remains a persistent source of uncertainty across a broad spectrum of glaciological research. Resolving bed elevation at an appropriate scale is necessary to investigate the spatial distributions and sensitivities of basal ice temperature, subglacial melting, water flow and ponding. For example, current geothermal heat flow (GHF) models for Antarctica resolve variability at scales $>10^3$ s of kilometres (Reading et al., 2022), resulting in model estimates that over half the Antarctic Ice Sheet bed is at the pressure melting point (Pattyn, 2010; Van Liefferinge and Pattyn, 2013). However, spatial variability in GHF at <10 km-scales modulated by bed roughness can induce local GHF variations up to twice the regional value (Colgan et al., 2021; van der Veen et al., 2007). Modelling investigations show that locally-varying GHF fields produce more meltwater than a constant GHF representing the regional mean (McCormack et al., 2022). Beneath inland ice there is insignificant frictional heating from basal sliding, amplifying the importance of GHF for basal ice temperatures.

Dome Fuji, inland East Antarctica is a candidate site for the preservation of ice over 1.5 Ma that could provide continuous climate records spanning the mid-Pleistocene Transition (Fischer et al., 2013). Constraints on GHF and subglacial hydrology are crucial in this region for characterising 1.5 Ma ice and understanding catchment-scale ice dynamics. At the interior of ice sheets where ice surfaces are relatively flat, bed topography mostly controls meltwater drainage (Shreve, 1972). Basal meltwater flows in extensive drainage networks (Dow et al., 2022), is stored in and released from subglacial lakes (Livingstone et al., 2022), and accretes onto the base of the ice sheet (Bell et al., 2011). Here, we compiled multiple ice-penetrating radar datasets to constrain ice thicknesses and investigate the bed beneath Dome Fuji (Figure 1a). The region has complex topography with mountains and valleys (Karlsson et al., 2018; Tsutaki et al., 2022), evidence for subglacial lakes (Karlsson et al., 2018; Popov and Masolov, 2007; Siegert, 2000), and estimated near-basal temperatures at the pressure melting point (Talalay et al., 2020). This indicates a potential for sensitive basal conditions and active hydrological systems, emphasizing the need for constraining the impacts of topographic variability and uncertainty.

2 Methods

2.1 Ice thickness data

Ice-thickness data were compiled from (Figure 1a): ground-survey data collected by a Japan-US-Norway collaboration and processed by the Centre for Remote Sensing of Ice Sheets (CReSIS), University of Kansas (Rodriguez-Morales et al., 2020); ground-survey data collected since 1992 by Japan's National Institute of Polar Research (NIPR) during Japanese Antarctic Research Expedition (JARE) 33-60 (Tsutaki et al., 2021a-i); airborne geophysical surveys conducted by the Alfred Wegener Institute's (AWI) Oldest Ice Reconnaissance (OIR) campaign (Eisen et al., 2020) and Geodynamic Evolution of East Antarctica (GEA) project (Eagles et al., 2021). At locations where data are not available within 10 km, background values were supplied by extracting Bedmap2 (Fretwell et al., 2013) data points and sampling BedMachine2.0 (Morlighem et al., 2020). See Supporting Information S1.1 for full details.

Two-way travel time to depth conversions for ice-bed picks were standardised (*Supporting Information S1.2*) between datasets using a radio-wave propagation speed of $1.69 \times 10^8 \text{ m s}^{-1}$, a depth-averaged assumption applied previously in this region (Tsutaki et al., 2022). The ice-thickness datasets were compared at 783 crossover points, yielding median differences - 1 m, 3 m, 18 m between CReSIS data and AWI, JARE59, JARE60 respectively (*Supporting Information S1.3*).

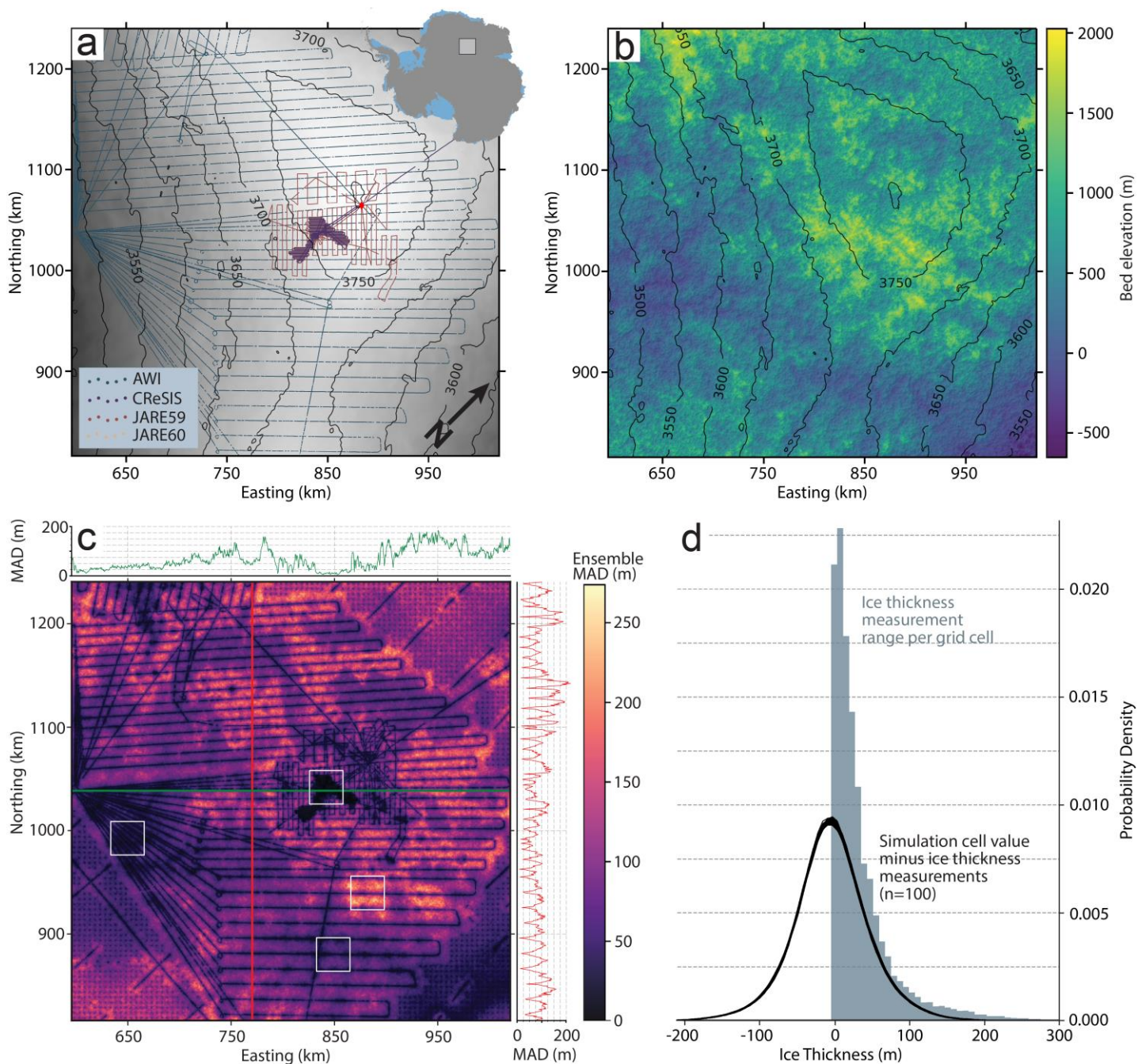


Figure 1. Bed topography simulations and analysis. **a)** Radar survey tracks, Dome Fuji Station (red diamond) and REMA ice surface contours (Howat et al., 2019). **b)** Hillshaded bed simulation #001 from the ensemble. **c)** Median absolute deviation (MAD) between 100 results with vertical and horizontal profiles plotted. Four boxes indicate sample locations (Section 4.3). **d)** Simulated bed minus measured ice thickness (100 curves) and measurement range within each map grid cell (bars). All maps projected to EPSG: 3031 with elevations in meters referenced to the WGS84 ellipsoid.

2.2 Stochastic simulation of bed topography

Sequential Gaussian Simulation (SGS) is a stochastic method (Deutsch and Journel, 1997) that can be applied to simulate values between measurements based on the statistical characteristics of nearby data (e.g. Graham et al., 2017; Law et al., 2023; MacKie et al., 2021, 2020). The SGS algorithm moves sequentially over a random path on a 2D grid, selecting values for unsurveyed grid cells using a Gaussian probability function. The probability distribution is generated using a local mean and semi-variogram estimated from a statistical model, and conditioned by surrounding data points which are sequentially updated with previously simulated values. We empirically determined optimum parameters for the exponential model based on the experimental semi-variogram (*Supporting Information S2*).

Ice-thickness data were decimated to 100 m spacing using a median reduction filter, and the SGS algorithm was implemented using 40 nearby conditioning data points within a search radius of 30 km to simulate values for cells without measurements. We used SGS to generate an ensemble of 100 ice-thickness grids, and bed elevation was estimated by subtracting ice thicknesses from the Reference Elevation Model of Antarctica (REMA) ice-surface elevation (Howat et al., 2019).

2.3 Topographic modification of geothermal heat flow

To simulate the impacts of topographic relief on GHF distribution, an adjustment factor for large-scale GHF fields was calculated following an empirical geostatistical approach (Colgan et al., 2021). A function for the unitless local topographic modification to GHF ($\Delta G/G$) was calculated:

$$\left(\frac{\Delta G}{G}\right)_{i,j} = \frac{1}{\alpha} (\bar{z}_{i,j} - z_{i,j}), \quad (1)$$

where G = modelled large-scale GHF estimate, α = empirically-determined local topographic relief required to induce 100% change in local GHF, z = local bed elevation, \bar{z} = mean elevation averaged over an empirically determined horizontal radius r , and i, j = two-dimensional horizontal grid indices. We used parameterisations $\alpha = 950$ m and $r = 5$ km based on a synthesis of parameter combinations against both observed and modelled local GHF anomalies that arise from topographic relief (Colgan et al., 2021).

2.4 Subglacial water flow and ponding

Subglacial hydraulic pressure potential (ϕ) was estimated for each simulated bed following Shreve (1972). We assumed that water pressure equals ice overburden pressure, a steady-state assumption appropriate for inland Antarctica where high-pressure distributed water systems are generally maintained between channels (Dow et al., 2022). Water routing was determined for gradients in ϕ using a D ∞ algorithm (Tarboton, 1997). Locations of hydraulic sinks were used to predict potential sites of subglacial lakes, and spill points provided a proxy for lake depths. Hydraulic sinks generated through stochastic simulation can be artificial at grid cells far from measurements, so median lake depth over the ensemble was used to screen for persistently predicted sites of water ponding.

3 Results

3.1 Bed elevation, variability and uncertainty

We generated an ensemble of $n = 100$ ice thickness and bed elevation grids (Shackleton et al., 2023) which have elevations between -500 m and 2100 m. An example result (#001) is presented in Figure 1b and all results are presented in Movie S1. Steep, mountainous terrain with valleys and ridges occurs at a subglacial massif south of Dome Fuji Station, with smoother terrain directly beneath and north of the ice dome and in lowland valleys converging to the southwest. Regional subglacial topography described in previous work (Fujita et al., 2012; Karlsson et al., 2018; Tsutaki et al., 2022) are observed in the results.

The median absolute deviation (MAD) for the bed topography ensemble stack quantifies the variability between simulated topography (Figure 1c) and has a regional average of 85 ± 41 m (mean $[\mu] \pm 1$ standard deviation $[\sigma]$). Areas with radar data are distinct with low MAD, with close to zero variability near dense survey profiles over the subglacial massif, and less than 25 m in the vicinity of other survey profiles. Less than 50 m variability is typically observed within 2 km of measurements, increasing to over 250 m between the most widely spaced survey profiles (10 km spacing). Measured topographic variability also influences MAD, which is high close to rough bed and generally below 100 m in smoother regions.

Individual results were validated by calculating the difference between ice-thickness measurements (before median filter decimation) and simulated ice-thickness grid cell values extracted at measurement locations (*Supporting Information S3.1*). Probability density functions for all validation results show little variability (Figure 1d), indicating that error distributions remain consistent across the ensemble. The ensemble mean difference is close to zero but distributed widely (0.9 ± 50.7 m). However, the range of observed ice-thickness within each grid cell is comparable at 37.2 ± 44 m (Figure 1d), suggesting that the uncertainty of simulated topography is similar to measured variability within individual grid cells.

3.2 Topography-adjusted geothermal heat flow

Bed topography grids were used to estimate local topographic adjustments to GHF (Shackleton et al., 2023), calculating a unitless adjustment factor $\Delta G/G$ for large-scale GHF fields (Figure 2a; Movie S2). The adjustment factor can be $\pm 40\%$ in regions with high topographic relief, with little to no adjustment in regions of smooth bed. At 10's of km-scale, adjustments show GHF is reduced along ridges and increased along valley floors (Figure 2b). The probability density functions for adjustment factors over ensemble results show negligible variation (Figure 2c) reflecting consistent regional roughness patterns. The regional impact of topographic adjustments therefore remains consistent between results, and ensemble median of 0.6% suggests elevated GHF is expected, with local adjustments mostly $\pm 20\%$ (2σ).

Regional GHF estimates differ substantially between published pan-Antarctic models, as shown in Figure S8 (An et al., 2015; Burton-Johnson et al., 2020; Lösing and Ebbing, 2021; Martos et al., 2017; Purucker, 2012; Shen et al., 2020; Stål et al., 2021). At Dome Fuji Station values range 40.0 - 63.7 mW m⁻² (Figure 2d). Our topographic GHF adjustments at the core site are between -6.5% and 10.2% over the ensemble (Figure 2e) but are predominantly positive at $2.8 \pm 3.1\%$ (1σ). By applying this adjustment factor to a local GHF of 78.9 ± 5.0 mW m⁻² estimated from borehole temperatures (Talalay et al., 2020), we inversely estimate an adjusted regional value of 76.7 mW m⁻² in the vicinity of Dome Fuji Station.

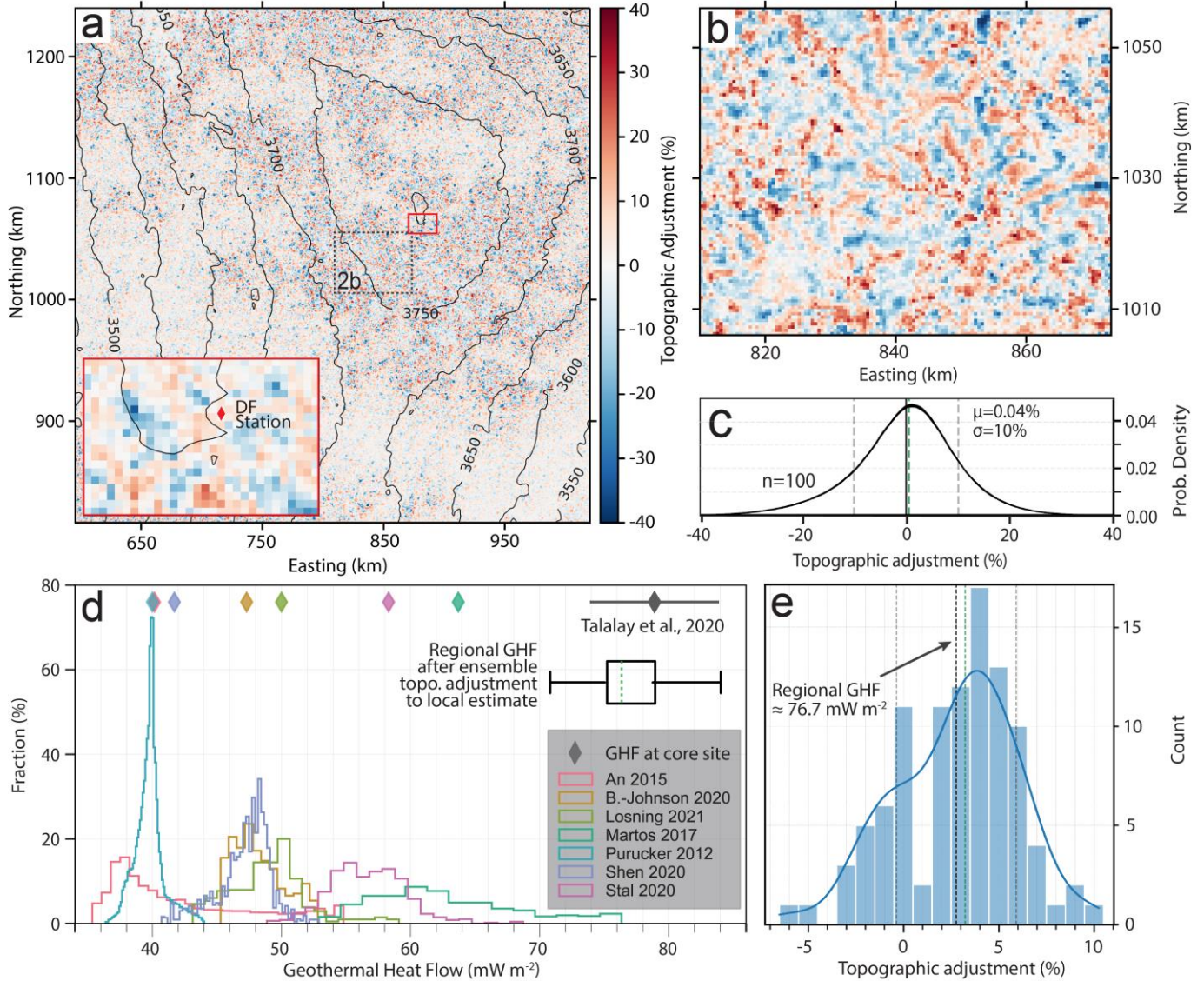


Figure 2. Spatial variations in GHF. a) Topographic adjustments to GHF (result #001) and inset a 10 x 15 km region (red box) around Dome Fuji Station. b) The central subglacial massif (result #001). c) Probability density curves for 100 topographic adjustment results, with ensemble-averaged standard deviation (grey), mean (black) and median (green). d) GHF distributions in the study region from pan-Antarctic models and corresponding value at Dome Fuji Station (diamonds). Local GHF estimate (Talalay et al., 2020) in grey, with box plot showing potential regional GHF range after ensemble adjustments to local value. e) Topographic adjustment factor over the ensemble at Dome Fuji Station, with ensemble-averaged mean (black), median (green) and standard deviation (grey).

3.3 Meltwater drainage and subglacial lakes

Our analysis predicts dendritic networks of streams routing water away from central sectors and the subglacial massif, broadly conforming to ice drainage divides at the regional scale and mostly following bed topography at <10 km scale (Figure 3). Dense grouping of predicted streams indicates consistent water-flow predictions, more commonly associated to regions with dense measurements for example at lower elevations in ice-drainage basin-3 (B3 in Figure 3). Spatially distributed stream predictions are ubiquitous and occur between otherwise stable stream networks, for example at Easting 700 km, Northing 1050 km where inconsistent water routing coincides with a larger gap between survey profiles (Figure 1a). Other regions contain inconsistent water routing despite regular spacing between profiles, coinciding with high topographic uncertainty where streams diverge around an obstacle (e.g., northern B10) and low topographic uncertainty within lowlands (e.g., southern divide of B3/B10). Ensemble analysis indicates potential sites for subglacial lakes at the bed which have ensemble median depths up to 27 m and extents ranging from 0.25 – 395 km². Using ensemble median values excludes infrequently predicted lakes in interpolated regions, resulting in more lakes near survey profiles.

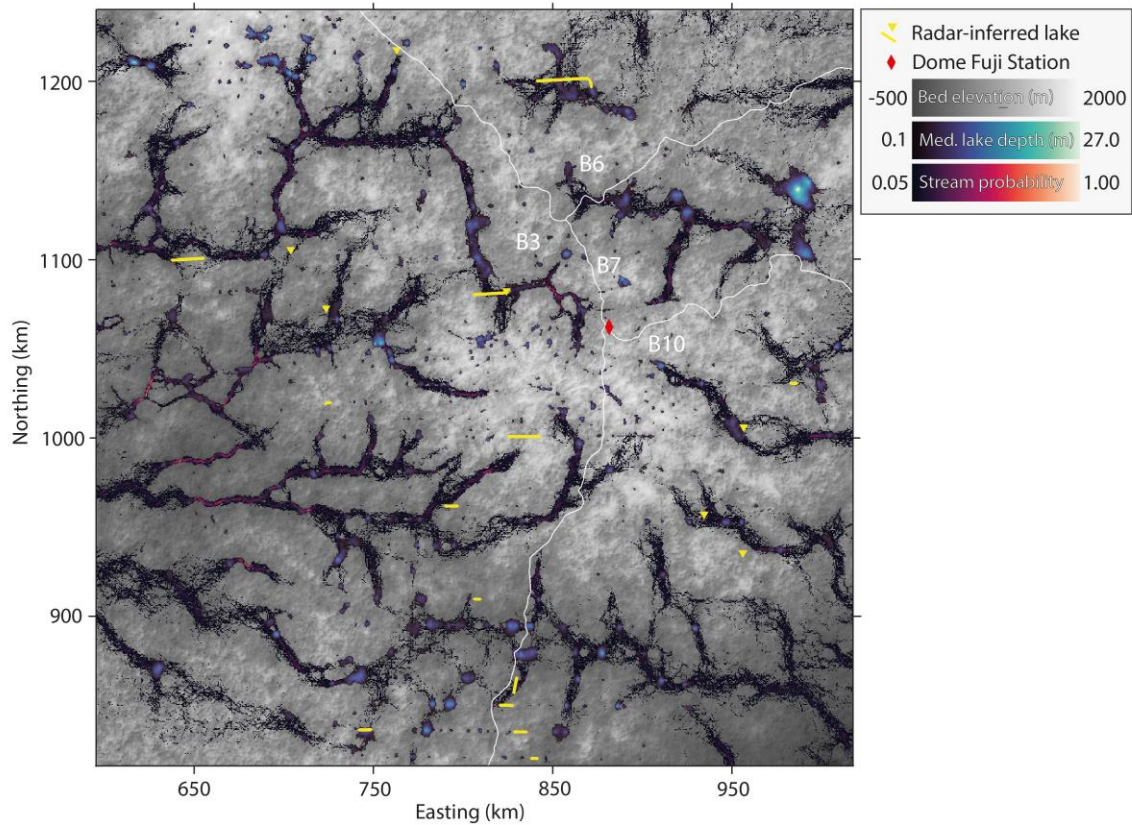


Figure 3. Subglacial drainage predicted over the bed topography ensemble. Stream probability (> 0.05) and ensemble median lake depths (> 0.1 m) over a hillshaded bed elevation map (result #001). Radar-inferred subglacial lakes as yellow triangles at lake center coordinates (Siebert et al., 2005) or lines along-profile (Karlsson et al., 2018). Ice sheet drainage basins delineated and labelled in white from Zwally et al., (2012).

4 Discussion

4.1 Topographic variability and subglacial processes

All topographic features with scales of 10's km are consistently observed across the ensemble, and regional patterns of GHF adjustments and subglacial water drainage remain consistent. The exact geometry and location of <10 km-scale topography can vary between simulations (Movie S1) and local-scale features are affected by topographic uncertainty (Figures 2a, 3), which is highest where the bed is rougher and/or measurement density is lower (Figure 1c). To examine variability in short-scale bed roughness we calculated the Terrain Ruggedness Index (TRI), which takes the square root of sum of squared differences between grid cells and 8 surrounding cells (Riley et al., 1999). Region-wide TRI has consistent distributions between simulated beds (Figure 4a), with ensemble median 213 ± 117 m (1σ). The regional mean TRI for the same domain in Bedmachine v3 is 34 ± 28 m (1σ) and Bedmap2 is 46 ± 36 m (1σ), suggesting that bed topography in this region could be an order-of-magnitude rougher with larger GHF variability than shown in other interpolated bed topography maps.

Subglacial drainage analyses predict potential locations and extents of subglacial lakes and show drainage sensitivities to topographic uncertainty (Figure 3). There are 20 subglacial lakes inferred from radar data in this region (Karlsson et al., 2018; Livingstone et al., 2022; Wright and Siegert, 2012), of which 11 directly coincide with our ensemble median lake predictions. Radar-derived bed elevation inherently masks the bathymetry of radar-detected lakes, so the topography analysis in this study is unlikely to predict all radar-detected lakes in bankfull condition. Of the 9 radar-inferred lakes that are not predicted in this study, 4 are located upstream of consistently predicted streams which delineate drainage pathways. Uncertainty-constrained subglacial water flow directions also outline any potential connectivity between drainage systems and across catchments that otherwise might not be detected using a single bed interpolation. We identified several drainage pathways across the continental ice-flow divides which reflect regionally low ice-surface slopes, and predicted lakes close to grid-south have uncertain drainage towards either Basin-3 or Basin-10. The topographic uncertainty analyses reveal regions where an ensemble approach to predicting subglacial processes could be necessary or more data is needed to reduce uncertainty, especially important in regions where basal conditions are sensitive to topographic variability.

4.2 Basal conditions and presence of 1.5 Ma old ice

Diagnosing basal conditions is crucial for deep ice core site selection, and our topographic adjustments to GHF show sensitivity to km-scale physiographic settings. Thermodynamical modelling suggests 3.1% of our study area had frozen bed for the past 1.5 Ma which could preserve old ice (Van Liefferinge et al., 2018). Regionally elevated GHF and local variability indicate that using large-scale GHF models may lead to inaccurate estimates of thawed bed and basal melt rates. The subglacial massif is well-constrained by measurements, and we consistently estimate local GHF adjustments up to $\pm 30\%$. The DF2 core was drilled in a locally elevated GHF region ca. 3% higher than background values, equating to 2.2 mW m^{-2} using the Talalay et al., (2020) estimate. Many localities even within 10 km of the previous site could have topographically adjusted GHF over 5% lower (Figure 2a), a crucial difference here where basal temperatures are close to or at the pressure melting point.

Over the subglacial massif, Van Liefferinge et al., (2018) estimated the threshold GHF required to keep basal ice frozen over the past 1.5 Ma is ca. 65 mW m^{-2} , which can be lowered to 55 mW m^{-2} considering new surface mass balance data averaged over the past 300 years (Van Liefferinge et al., 2021). Some pan-Antarctic models show that the revised threshold is met over the subglacial massif, but do not replicate local GHF derived from borehole-temperatures despite our topographic adjustment factor (Figure 2d). Previous borehole-based GHF estimates using an ice thickness of 3090 m reported earlier (Dome-F Deep Coring Group, 1998) were lower at 59 mW m^{-2} (Hondoh et al., 2002) and 50.4 mW m^{-2} (Mony et al., 2020). A revised ice thickness of 3028 ± 15 (Fujita et al., 2006) was used by Talalay et al., (2020) for their estimate of $78.9 \pm 5.0 \text{ mW m}^{-2}$. Our data compilation suggests radar-derived ice thicknesses within 500 m of the DF1 core site are $3018 \pm 16 \text{ m}$ (1σ), based on averaged values from 4 independent surveys (Table S2), supporting the larger GHF estimates around Dome Fuji Station.

Simulated bed topography with robust uncertainty constraints indicate that local relief is not a significant control on the current ice dome location, implying that the location could have been different in the past. Thermomechanical modelling suggests that ice thicknesses could have fluctuated up to 250 m near Dome Fuji over the last 800 ka (Parrenin et al., 2007). Re-routing of water between catchments is plausible with shifting overlying ice, and historical water storage and drainage patterns could vary significantly from present-day conditions, which could affect delineation and characterisation of 1.5 Ma old ice. Meltwater refreezing onto basal ice also has significant potential to disturb basal ice stratigraphy, as observed in the nearby Gamburtsev Mountains (Bell et al., 2011). Our bed topography ensemble could be utilised further to constrain potential basal ice flow disturbances to layer stratigraphy through ice flow modelling.

4.3 Survey spacing required for a given bed uncertainty tolerance

The wide-ranging radar survey spacings in this region (0.25 - 10 km) allowed us to explore the relationship between distance d from radar data, bed roughness (TRI), and topographic uncertainty (MAD). Based on ensemble-averaged TRI and survey locations we manually identified regions that have characteristically rough and smooth bed with both dense and sparse measurements (Figure 1c: white boxes). TRI in these regions is distinct across the ensemble (Figure 4a). MAD increases for increasing d but plateaus for $d > 6 \text{ km}$, at ca. 200 m for rough bed and ca. 75 m for smooth bed (Figure 4b). Both examples with distinct data density show similar distance dependencies for MAD, which implies a bed-roughness-dependent relationship between topographic uncertainty and survey spacing. Regression analysis between TRI and MAD for data grouped into 0.5 km d intervals for $0 \text{ km} < d < 10 \text{ km}$ (Figure 4c) demonstrates that MAD increases with TRI for each d interval, and the rate of increase is enhanced for larger d . Linear models were fit to binned data with y-intercept fixed at zero assuming MAD approaches zero for smooth surfaces, showing that $\text{MAD} \approx \beta \text{TRI}$, where β represents the dependence of topographic uncertainty on bed roughness.

302

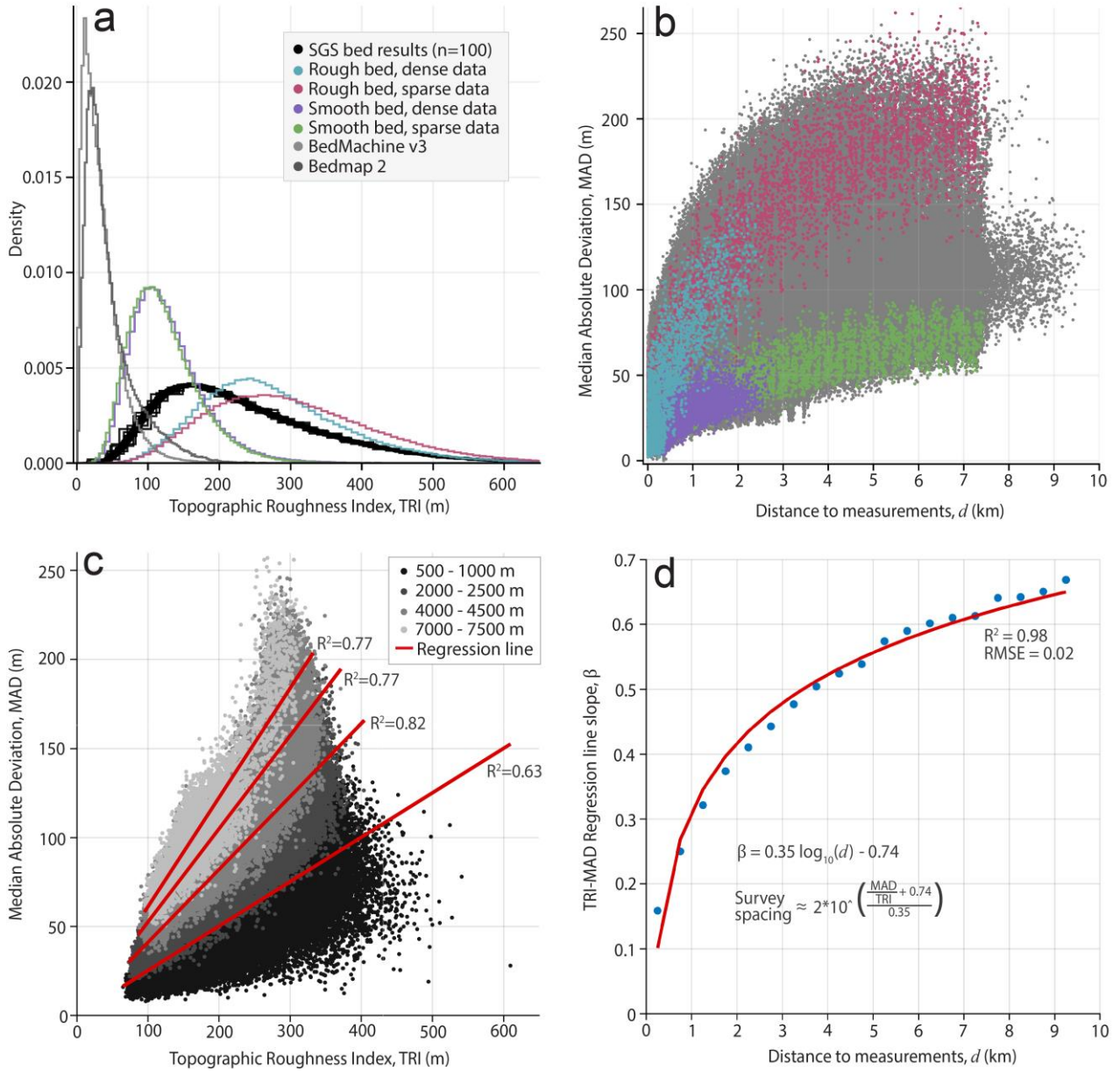


Figure 4: Topographic uncertainty dependence on bed roughness and survey spacing. **a)** Topographic Roughness Index (TRI) in the Dome Fuji region, for ensemble results (black curves), sample regions shown in Figure 1c, Bedmachine v3, and Bedmap2 at native resolution. **b)** Median Absolute Deviation (MAD) at increasing distances from measurements. Characteristic regions plotted in same colours as 4a, with all other locations in gray. **c)** MAD for increasing TRI binned at 0.5 km d intervals between 0 and 10 km. Only 4 of the 19 intervals are plotted to show overall trends, with full model statistics in Table S3. **d)** Slopes of fitted regression lines in 4c, at increasing distance to measurements.

311

312

Figure 4d shows the distance dependence for β , and the empirical relationship could be used to guide survey planning given an initial estimate for regional roughness based on existing data or preliminary surveys. Interpolated grids based on sparse data lack roughness between survey profiles and are not suitable for preliminary roughness analyses. Using a derived TRI, the separation between survey profiles (i.e. twice the distance to data points, $2d$) can be prescribed for a given uncertainty tolerance (Figure 4d). If bed roughness is similar to the Dome Fuji region (median TRI = 213 m), survey profiles should be separated by 1.2 km, 5.7 km, 27 km for an uncertainty tolerance of 50 m, 100 m, 150 m respectively. Considering TRI σ of 117 m the previous survey spacings are reduced to 0.7 km, 1.9 km, 14 km however for TRI of 330 m. Although it is difficult to accurately estimate bed roughness prior to extensive surveys, this relationship could be used to empirically implement scientific requirements into survey planning. Bed topography mapping guided by uncertainty tolerance might be particularly useful in coastal regions of Antarctica, where uncertainty could impact estimated ice discharge and projected grounding-line retreat of fast-flowing glaciers. To develop this approach further the measurement scale and bed roughness metric should be investigated as well as the impacts of grid cell size. New pan-Antarctic datasets (Frémand et al., 2022) could facilitate analyses of this relationship for different regions and glaciological settings.

5 Conclusions

Stochastic simulations provided detailed bed topography with realistic roughness an order-of-magnitude larger than previous interpolations. Topographic uncertainty is significantly larger in regions with rougher bed, and we quantified the dependence of topographic uncertainty on distance to radar measurements and bed roughness. An empirical relationship can guide the spacings of future surveys in the Dome Fuji region and could be applied and developed elsewhere to plan surveys within a framework of uncertainty tolerance. Constraining the bed to within 50 m requires radar profile spacings of 0.7 km to 1.2 km in this region. The impacts of topographic variability on the distribution of GHF and subglacial drainage were investigated through ensemble analysis of simulated beds. Topographically adjusted GHF is elevated in valleys and reduced over ridges, with km-scale variability leading to widespread local GHF adjustments $\pm 20\%$ the regional value, aggregating to enhance overall GHF. These effects could strongly regulate the distribution of basal ice at the pressure melting point and should be included in future estimates. Hydraulic potential analysis reveals meltwater drainage pathways and their relative probability, which maps water discharge from subglacial lakes and basal melt from the upper regions of ice-flow catchments, as well as highlighting regions potentially sensitive to ice dome migration. Our analysis indicates widespread potential for subglacial lakes in the region, which coincide with over half of the lake locations proposed in previous work and identify potential locations of undetected lakes. This uncertainty-constrained drainage analysis and GHF adjustment approach is useful in the Dome Fuji region and could be applied elsewhere to diagnose basal conditions and delineate 1.5 Ma old ice.

366 Data availability

374 **References**

- 13

- CReSIS Toolbox* (3.0.1). (2021). [Software]. Centre for Remote Sensing of Ice Sheets (CReSIS).
doi.org/10.5281/zenodo.5683959
- Deutsch, C. V., & Journel, A. G. (1997). *GSLIB: Geostatistical software library and user's guide*. (Second Edition). New York: Oxford University Press.
- Dow, C. F., Ross, N., Jeofry, H., Siu, K., & Siegert, M. J. (2022). Antarctic basal environment shaped by high-pressure flow through a subglacial river system. *Nature Geoscience*, 1–7.
doi.org/10.1038/s41561-022-01059-1
- Eagles, G., Ruppel, A., Jokat, W., & Läufer, A. (2021). *GEA IV 2013-15 radar ice thickness in eastern Dronning Maud Land* [Data set]. PANGAEA.
[doi.pangaea.de/10.1594/PANGAEA.938357](https://doi.org/10.1594/PANGAEA.938357)
- Eisen, O., Steinhage, D., Karlsson, N. B., Binder, T., & Helm, V. (2020). *Ice thickness of Dome Fuji region, Antarctica, recorded with the AWI airborne radar system: Line 20172023* [Data set]. PANGAEA. [doi.pangaea.de/10.1594/PANGAEA.920619](https://doi.org/10.1594/PANGAEA.920619)
- Fischer, H., Severinghaus, J., Brook, E., Wolff, E., Albert, M., Alemany, O., Arthern, R., Bentley, C., Blankenship, D., Chappellaz, J., Creyts, T., Dahl-Jensen, D., Dinn, M., Frezzotti, M., Fujita, S., Gallee, H., Hindmarsh, R., Hudspeth, D., Jugie, G., ... Wilhelms, F. (2013). Where to find 1.5 million yr old ice for the IPICS ‘Oldest-Ice’ ice core. *Climate of the Past*, 9(6), 2489–2505. doi.org/10.5194/cp-9-2489-2013
- Frémand, A. C., Fretwell, P., Bodart, J., Pritchard, H. D., Aitken, A., Bamber, J. L., Bell, R., Bianchi, C., Bingham, R. G., Blankenship, D. D., Casassa, G., Catania, G., Christianson, K., Conway, H., Corr, H. F. J., Cui, X., Damaske, D., Damm, V., Drews, R., ... Zirizzotti, A. (2022). Antarctic Bedmap data: FAIR sharing of 60 years of ice bed, surface and thickness data. *Earth System Science Data Discussions*, 1–25.
doi.org/10.5194/essd-2022-355
- Fretwell, P., Pritchard, H. D., Vaughan, D. G., Bamber, J. L., Barrand, N. E., Bell, R., Bianchi, C., Bingham, R. G., Blankenship, D. D., Casassa, G., Catania, G., Callens, D., Conway, H., Cook, A. J., Corr, H. F. J., Damaske, D., Damm, V., Ferraccioli, F., Forsberg, R., ... Zirizzotti, A. (2013). Bedmap2: Improved ice bed, surface and thickness datasets for Antarctica. *Cryosphere*, 7(1), 375–393. doi.org/10.5194/tc-7-375-2013
- Fujita, S., Holmlund, P., Matsuoka, K., Enomoto, H., Fukui, K., Nakazawa, F., Sugiyama, S., & Surdyk, S. (2012). Radar diagnosis of the subglacial conditions in Dronning Maud Land, East Antarctica. *The Cryosphere*, 6(5), 1203–1219. doi.org/10.5194/tc-6-1203-2012
- Fujita, S., Maeno, H., & Matsuoka, K. (2006). Radio-wave depolarization and scattering within ice sheets: A matrix-based model to link radar and ice-core measurements and its application. *Journal of Glaciology*, 52(178), 407–424.
doi.org/10.3189/172756506781828548
- Graham, F. S., Roberts, J. L., Galton-Fenzi, B. K., Young, D., Blankenship, D., & Siegert, M. J. (2017). A high-resolution synthetic bed elevation grid of the Antarctic continent. *Earth System Science Data*, 9(1), 267–279. doi.org/10.5194/essd-9-267-2017
- Hondoh, T., Shoji, H., Watanabe, O., Salamat, A. N., & Lipenkov, V. Y. (2002). Depth–age and temperature prediction at Dome Fuji station, East Antarctica. *Annals of Glaciology*, 35, 384–390. doi.org/10.3189/172756402781817013

- Howat, I. M., Porter, C., Smith, B. E., Noh, M.-J., & Morin, P. (2019). The Reference Elevation Model of Antarctica. *The Cryosphere*, 13(2), 665–674. doi.org/10.5194/tc-13-665-2019
- Kapitsa, A. P. (1964). New data on ice thickness in the central regions of Antarctica. *Soviet Antarctic Expedition Bulletin*, 2, 247–250.
- Karlsson, N. B., Binder, T., Eagles, G., Helm, V., Pattyn, F., Liefveringe, B. V., & Eisen, O. (2018). Glaciological characteristics in the Dome Fuji region and new assessment for ‘Oldest Ice’. *Cryosphere*, 12(7), 2413–2424. doi.org/10.5194/tc-12-2413-2018
- Kawamura, K., Abe-Ouchi, A., Motoyama, H., Ageta, Y., Aoki, S., Azuma, N., Fujii, Y., Fujita, K., Fujita, S., Fukui, K., Furukawa, T., Furusaki, A., Goto-Azuma, K., Greve, R., Hirabayashi, M., Hondoh, T., Hori, A., Horikawa, S., Horiuchi, K., ... Yoshimoto, T. (2017). State dependence of climatic instability over the past 720,000 years from Antarctic ice cores and climate modeling. *Science Advances*, 3(2), e1600446. doi.org/10.1126/sciadv.1600446
- Kawamura, K., Nakazawa, T., Aoki, S., Sugawara, S., Fujii, Y., & Watanabe, O. (2003). Atmospheric CO₂ variations over the last three glacial/interglacial climatic cycles deduced from the Dome Fuji deep ice core, Antarctica using a wet extraction technique. *Tellus B: Chemical and Physical Meteorology*, 55(2), 126–137. doi.org/10.3402/tellusb.v55i2.16730
- Law, R., Christoffersen, P., MacKie, E., Cook, S., Haseloff, M., & Gagliardini, O. (2023). Complex motion of Greenland Ice Sheet outlet glaciers with basal temperate ice. *Science Advances*, 9(6), eabq5180. doi.org/10.1126/sciadv.abq5180
- Livingstone, S. J., Li, Y., Rutishauser, A., Sanderson, R. J., Winter, K., Mikucki, J. A., Björnsson, H., Bowling, J. S., Chu, W., Dow, C. F., Fricker, H. A., McMillan, M., Ng, F. S. L., Ross, N., Siegert, M. J., Siegfried, M., & Sole, A. J. (2022). Subglacial lakes and their changing role in a warming climate. *Nature Reviews Earth & Environment*, 1–19. doi.org/10.1038/s43017-021-00246-9
- Lösing, M., & Ebbing, J. (2021). Predicting Geothermal Heat Flow in Antarctica With a Machine Learning Approach. *Journal of Geophysical Research: Solid Earth*, 126(6), e2020JB021499. doi.org/10.1029/2020JB021499
- MacKie, E. J., Schroeder, D. M., Caers, J., Siegfried, M. R., & Scheidt, C. (2020). Antarctic Topographic Realizations and Geostatistical Modeling Used to Map Subglacial Lakes. *Journal of Geophysical Research: Earth Surface*, 125(3), e2019JF005420. doi.org/10.1029/2019JF005420
- MacKie, E. J., Schroeder, D. M., Zuo, C., Yin, Z., & Caers, J. (2021). Stochastic modeling of subglacial topography exposes uncertainty in water routing at Jakobshavn Glacier. *Journal of Glaciology*, 67(261), 75–83. doi.org/10.1017/jog.2020.84
- MacKie, E., Field, M., Wang, L., Yin, Z., Schoedl, N., & Hibbs, M. (2022). [Software] *GStatSim*. Zenodo. doi.org/10.5281/zenodo.7230276
- Martos, Y. M., Catalán, M., Jordan, T. A., Golynsky, A., Golynsky, D., Eagles, G., & Vaughan, D. G. (2017). Heat Flux Distribution of Antarctica Unveiled. *Geophysical Research Letters*, 44(22), 11,417–11,426. doi.org/10.1002/2017GL075609

- McCormack, F. S., Roberts, J. L., Dow, C. F., Stål, T., Halpin, J. A., Reading, A. M., & Siegert, M. J. (2022). Fine-Scale Geothermal Heat Flow in Antarctica Can Increase Simulated Subglacial Melt Estimates. *Geophysical Research Letters*, 49(15), e2022GL098539. doi.org/10.1029/2022GL098539
- Mälicke, M., Möller, E., Schneider, H. D., & Müller, S. (2021). [Software] scikit-gstat: A scipy flavoured geostatistical variogram analysis toolbox. *Zenodo*. doi.org/10.5281/zenodo.4835779
- Mony, L., Roberts, J. L., & Halpin, J. A. (2020). Inferring geothermal heat flux from an ice-borehole temperature profile at Law Dome, East Antarctica. *Journal of Glaciology*, 66(257), 509–519. doi.org/10.1017/jog.2020.27
- Morlighem, M., Rignot, E., Binder, T., Blankenship, D., Drews, R., Eagles, G., Eisen, O., Ferraccioli, F., Forsberg, R., Fretwell, P., Goel, V., Greenbaum, J. S., Gudmundsson, H., Guo, J., Helm, V., Hofstede, C., Howat, I., Humbert, A., Jokat, W., ... Young, D. A. (2020). Deep glacial troughs and stabilizing ridges unveiled beneath the margins of the Antarctic ice sheet. *Nature Geoscience*, 13(2), Article 2. doi.org/10.1038/s41561-019-0510-8
- Motoyama, H., Takahashi, A., Tanaka, Y., Shinbori, K., Miyahara, M., Yoshimoto, T., Fujii, Y., Furusaki, A., Azuma, N., Ozawa, Y., Kobayashi, A., & Yoshise, Y. (2021). Deep ice core drilling to a depth of 3035.22 m at Dome Fuji, Antarctica in 2001–07. *Annals of Glaciology*, 62(85–86), 212–222. doi.org/10.1017/aog.2020.84
- Parrenin, F., Dreyfus, G., Durand, G., Fujita, S., Gagliardini, O., Gillet, F., Jouzel, J., Kawamura, K., Lhomme, N., Masson-Delmotte, V., Ritz, C., Schwander, J., Shoji, H., Uemura, R., Watanabe, O., & Yoshida, N. (2007). 1-D-ice flow modelling at EPICA Dome C and Dome Fuji, East Antarctica. *Climate of the Past*, 3(2), 243–259. doi.org/10.5194/cp-3-243-2007
- Pattyn, F. (2010). Antarctic subglacial conditions inferred from a hybrid ice sheet/ice stream model. *Earth and Planetary Science Letters*, 295(3), 451–461. doi.org/10.1016/j.epsl.2010.04.025
- Popov, S. V., & Masolov, V. N. (2007). Forty-seven new subglacial lakes in the 0–110° E sector of East Antarctica. *Journal of Glaciology*, 53(181), 289–297. doi.org/10.3189/172756507782202856
- Purucker, M. (2012). Geothermal heat flux data set based on low resolution observations collected by the CHAMP satellite between 2000 and 2010, and produced from the MF-6 model following the technique described in Fox Maule et al. (2005). http://websrv.cs.umn.edu/isis/index.php/Main_Page
- Pyrzcz, M., Jo, H., Kuppenko, A., Liu, W., Gigliotti, A. E., Salomaki, T., & Javier, S. (2021). [Software] *GeostatsPy: Geostatistical Library in Python* (1.0.0). doi.org/10.5281/zenodo.
- Reading, A. M., Stål, T., Halpin, J. A., Lösing, M., Ebbing, J., Shen, W., McCormack, F. S., Siddoway, C. S., & Hasterok, D. (2022). Antarctic geothermal heat flow and its implications for tectonics and ice sheets. *Nature Reviews Earth & Environment*, 1–18. doi.org/10.1038/s43017-022-00348-y

- Riley, S. J., DeGloria, S. D., & Elliot, R. (1999). Index that quantifies topographic heterogeneity. *Intermountain Journal of Sciences*, 5(1–4), 23–27.
- Rodriguez-Morales, F., Braaten, D., Mai, H. T., Paden, J., Gogineni, P., Yan, J. B., Abe-Ouchi, A., Fujita, S., Kawamura, K., Tsutaki, S., Liefferinge, B. V., Matsuoka, K., & Steinhage, D. (2020). A Mobile, Multichannel, UWB Radar for Potential Ice Core Drill Site Identification in East Antarctica: Development and First Results. *IEEE Journal of Selected Topics in Applied Earth Observations and Remote Sensing*, 13, 4836–4847. doi.org/10.1109/JSTARS.2020.3016287
- Shackleton, C., Matsuoka, K., Moholdt, G., Paden, J., & Van Liefferinge, B. (2023). Ice thickness, bed elevation, and topographic adjustments to geothermal heat flow near Dome Fuji, East Antarctica [Data set]. *Norwegian Polar Institute*. doi.org/10.21334/NPOLAR.2023.DBD63194
- Shen, W., Wiens, D. A., Lloyd, A. J., & Nyblade, A. A. (2020). A Geothermal Heat Flux Map of Antarctica Empirically Constrained by Seismic Structure. *Geophysical Research Letters*, 47(14), e2020GL086955. doi.org/10.1029/2020GL086955
- Shreve, R. L. (1972). The movement of water in glaciers. *Journal of Glaciology*, 11(62), 205–214.
- Siegert, M. J. (2000). Antarctic subglacial lakes. *Earth Science Reviews*, 50(1–2), 29–50. doi.org/10.1016/S0012-8252(99)00068-9
- Stål, T., Reading, A. M., Halpin, J. A., & Whittaker, J. M. (2021). Antarctic Geothermal Heat Flow Model: Aq1. *Geochemistry, Geophysics, Geosystems*, 22(2), e2020GC009428. doi.org/10.1029/2020GC009428
- Talalay, P., Yazhou, L., Augustin, L., Clow, G., Hong, J., Lefebvre, E., Markov, A., Motoyama, H., & Ritz, C. (2020). Geothermal heat flux from measured temperature profiles in deep ice boreholes in Antarctica. *The Cryosphere*, 14, 4021–4037. doi.org/10.5194/tc-14-4021-2020
- Tarboton, D. G. (1997). A new method for the determination of flow directions and upslope areas in grid digital elevation models. *Water Resources Research*, 33(2), 309–319. doi.org/10.1029/96WR03137
- Tsutaki, S., Fujita, S., Kawamura, K., Abe-Ouchi, A., Fukui, K., Motoyama, H., Hoshina, Y., Nakazawa, F., Obase, T., Ohno, H., Oyabu, I., Saito, F., Sugiura, K., & Suzuki, T. (2021a). Ice thickness around Dome Fuji, Antarctica, based on JARE ground-based radar surveys: JARE33 data. *Arctic Data Archive System (ADS)*, 1.00(Japan). http://doi.org/10.17592/001.2021110909
- Tsutaki, S., Fujita, S., Kawamura, K., Abe-Ouchi, A., Fukui, K., Motoyama, H., Hoshina, Y., Nakazawa, F., Obase, T., Ohno, H., Oyabu, I., Saito, F., Sugiura, K., & Suzuki, T. (2021b). Ice thickness around Dome Fuji, Antarctica, based on JARE ground-based radar surveys: JARE37 data. *Arctic Data Archive System (ADS)*, 1.00(Japan). http://doi.org/10.17592/001.2021110909
- Tsutaki, S., Fujita, S., Kawamura, K., Abe-Ouchi, A., Fukui, K., Motoyama, H., Hoshina, Y., Nakazawa, F., Obase, T., Ohno, H., Oyabu, I., Saito, F., Sugiura, K., & Suzuki, T. (2021c). Ice thickness around Dome Fuji, Antarctica, based on JARE ground-based radar

- surveys: JARE40 data. *Arctic Data Archive System (ADS)*, 1.00(Japan).
<http://doi.org/10.17592/001.2021110909>
- Tsutaki, S., Fujita, S., Kawamura, K., Abe-Ouchi, A., Fukui, K., Motoyama, H., Hoshina, Y., Nakazawa, F., Obase, T., Ohno, H., Oyabu, I., Saito, F., Sugiura, K., & Suzuki, T. (2021d). Ice thickness around Dome Fuji, Antarctica, based on JARE ground-based radar surveys: JARE49 POL 179 MHz data. *Arctic Data Archive System (ADS)*, 1.00(Japan).
<http://doi.org/10.17592/001.2021110909>
- Tsutaki, S., Fujita, S., Kawamura, K., Abe-Ouchi, A., Fukui, K., Motoyama, H., Hoshina, Y., Nakazawa, F., Obase, T., Ohno, H., Oyabu, I., Saito, F., Sugiura, K., & Suzuki, T. (2021e). Ice thickness around Dome Fuji, Antarctica, based on JARE ground-based radar surveys: JARE49 VHF 60 MHz data. *Arctic Data Archive System (ADS)*, 1.00(Japan).
<http://doi.org/10.17592/001.2021110909>
- Tsutaki, S., Fujita, S., Kawamura, K., Abe-Ouchi, A., Fukui, K., Motoyama, H., Hoshina, Y., Nakazawa, F., Obase, T., Ohno, H., Oyabu, I., Saito, F., Sugiura, K., & Suzuki, T. (2021f). Ice thickness around Dome Fuji, Antarctica, based on JARE ground-based radar surveys: JARE54 data. *Arctic Data Archive System (ADS)*, 1.00(Japan).
<http://doi.org/10.17592/001.2021110909>
- Tsutaki, S., Fujita, S., Kawamura, K., Abe-Ouchi, A., Fukui, K., Motoyama, H., Hoshina, Y., Nakazawa, F., Obase, T., Ohno, H., Oyabu, I., Saito, F., Sugiura, K., & Suzuki, T. (2021g). Ice thickness around Dome Fuji, Antarctica, based on JARE ground-based radar surveys: JARE59 POL 179 MHz data. *Arctic Data Archive System (ADS)*, 1.00(Japan).
<http://doi.org/10.17592/001.2021110909>
- Tsutaki, S., Fujita, S., Kawamura, K., Abe-Ouchi, A., Fukui, K., Motoyama, H., Hoshina, Y., Nakazawa, F., Obase, T., Ohno, H., Oyabu, I., Saito, F., Sugiura, K., & Suzuki, T. (2021h). Ice thickness around Dome Fuji, Antarctica, based on JARE ground-based radar surveys: JARE59 VHF 179 MHz data. *Arctic Data Archive System (ADS)*, 1.00(Japan).
<http://doi.org/10.17592/001.2021110909>
- Tsutaki, S., Fujita, S., Kawamura, K., Abe-Ouchi, A., Fukui, K., Motoyama, H., Hoshina, Y., Nakazawa, F., Obase, T., Ohno, H., Oyabu, I., Saito, F., Sugiura, K., & Suzuki, T. (2021i). Ice thickness around Dome Fuji, Antarctica, based on JARE ground-based radar surveys: JARE60 data. *Arctic Data Archive System (ADS)*, 1.00(Japan).
<http://doi.org/10.17592/001.2021110909>
- Tsutaki, S., Fujita, S., Kawamura, K., Abe-Ouchi, A., Fukui, K., Motoyama, H., Hoshina, Y., Nakazawa, F., Obase, T., Ohno, H., Oyabu, I., Saito, F., Sugiura, K., & Suzuki, T. (2022). High-resolution subglacial topography around Dome Fuji, Antarctica, based on ground-based radar surveys over 30 years. *The Cryosphere*, 16(7), 2967–2983.
doi.org/10.5194/tc-16-2967-2022
- Uieda, L. (2018). Verde: Processing and gridding spatial data using Green’s functions. *Journal of Open Source Software*, 3(30), 957. doi.org/10.21105/joss.00957
- van der Veen, C. J., Leftwich, T., von Frese, R., Csatho, B. M., & Li, J. (2007). Subglacial topography and geothermal heat flux: Potential interactions with drainage of the Greenland ice sheet. *Geophysical Research Letters*, 34(12).
doi.org/10.1029/2007GL030046

- Van Liefferinge, B., & Pattyn, F. (2013). Using ice-flow models to evaluate potential sites of million year-old ice in Antarctica. *Climate of the Past*, 9, 2335–2345.
- Van Liefferinge, B., Pattyn, F., Cavitte, M. G. P., Karlsson, N. B., Young, D. A., Sutter, J., & Eisen, O. (2018). Promising oldest ice sites in east antarctica based on thermodynamical modelling. *Cryosphere*, 12(8), 2773–2787. doi.org/10.5194/tc-12-2773-2018
- Van Liefferinge, B., Taylor, D., Tsutaki, S., Fujita, S., Gogineni, P., Kawamura, K., Matsuoka, K., Moholdt, G., Oyabu, I., Abe-Ouchi, A., Awasthi, A., Buizert, C., Gallet, J.-C., Isaksson, E., Motoyama, H., Nakazawa, F., Ohno, H., O'Neill, C., Pattyn, F., & Sugiura, K. (2021). Surface Mass Balance Controlled by Local Surface Slope in Inland Antarctica: Implications for Ice-Sheet Mass Balance and Oldest Ice Delineation in Dome Fuji. *Geophysical Research Letters*, 48(24), e2021GL094966. doi.org/10.1029/2021GL094966
- Watanabe, O., Kamiyama, K., Motoyama, H., Fujii, Y., Shoji, H., & Satow, K. (1999). The paleoclimate record in the ice core at Dome Fuji station, East Antarctica. *Annals of Glaciology*, 29, 176–178. doi.org/10.3189/172756499781821553
- Wright, A., & Siegert, M. (2012). A fourth inventory of Antarctic subglacial lakes. *Antarctic Science*, 24(6), 1–6. doi.org/10.1017/S095410201200048X
- Zwally, H. J., Giovinetto, M. B., Beckley, M. A., & Saba, J. L. (2012). *Antarctic and Greenland Drainage Systems*. GSFC Cryospheric Sciences Laboratory; 610 Web Dev. <https://earth.gsfc.nasa.gov/cryo/data/polar-altimetry/antarctic-and-greenland-drainage-systems>

Supporting Information for:

Stochastic Simulations of Bed Topography Constrain Geothermal Heat Flow and Subglacial Drainage near Dome Fuji, East Antarctica

Calvin Shackleton^{1*}, Kenichi Matsuoka¹, Geir Moholdt¹, John Paden², Brice Van Liefferinge¹

¹ Norwegian Polar Institute, Fram Senteret, Tromsø, Norway, 9296

² Center for Remote Sensing of Ice Sheets (CReSIS), The University of Kansas, Lawrence, KS, USA, 66045

*calvin.shackleton@npolar.no

Contents of this file

Text S1 to S3.3

Figures S1 to S8

Tables S1 to S3

Additional Supporting Information (Files uploaded separately)

Captions for Movies S1 to S2

Introduction

Supporting text S1 provides additional details for individual ice thickness data sources (S1.1), the data calibration (S1.2), and crossover analysis (S1.3). S2 provides further detail on the stochastic simulation of bed topography (see section 2.2 in main text), including software and tools used (S2.1) and geostatistical model development and implementation into simulations (S2.2). S3 is an extended description of the results, including validation of simulated bed results (S3.1), geothermal heat flow models and topographic adjustments (S3.2), and model parameters for the bed roughness and uncertainty analysis (S3.3).

Text S1. Individual data sources and data standardization

S1.1 Ice-thickness data sources

The sources for all ice-thickness data used in this study are listed in Table S1, and the following text outlines any additional details and processing of available data:

CReSIS: Data are geolocated radar data (echograms).

JARE: Ice-thickness data collected between 1992 and 2008 (JARE33-49) had been calibrated to JARE59-60 surveys based on crossover error analysis (Tsutaki et al., 2022). We combined the older radar survey JARE 33-54 data collected between 1992 and 2013 and filtered out data if there were newer data from more recently conducted surveys (CReSIS, JARE59-60, AWI) within 500 m.

Bedmap2: Gridded ice-thickness data were extracted from the Bedmap2 ice-thickness grid using the survey coverage mask. Data were filtered out if there were any survey data (CReSIS, JARE33-60, AWI) within 10 km. This procedure yields only grid values based on data from the Soviet Antarctic Expedition (Kapitsa, 1964).

BedMachine: Gridded ice-thickness data were extracted from the BedMachine v2 ice-thickness grid by sampling across the Dome Fuji region at a uniform 2 km spacing to yield 6752 data points. The sampled data were then filtered out if they were within 10 km of radar-derived ice-thickness measurements (*CReSIS*, *JARE33-60*, *AWI*, *Bedmap2*). BedMachine v3 was released close to the end of our experiments, however, analysing differences between v3 and v2 in the Dome Fuji region at our 6752 sample points yielded differences with mean 0.6 m and standard deviation 9.2 m, suggesting negligible impacts on our results.

The study region is from 596 km to 1020 km Easting, 816 km to 1240 km Northing, on a Polar Stereographic projection parallel to 71°S (EPSG: 3031). We added a 100 km buffer to this region before clipping available data to prevent too few data being available close to the region boundary when running the stochastic simulations. Ice-thickness measurement data were then decimated to a minimum 100 m spacing using a median reduction filter. This removes some surplus data at the chosen resolution of 500 m and also reduces the likelihood of closely spaced measurements with large inconsistencies in thickness which could lead to misrepresented topographic roughness.

Table S1: Source of the radar data used for generating subglacial topography grids.

Institute/ data origin	Survey/Project name	Acquisition date	Source/DOI/key reference
Alfred Wegener Institute (AWI)	Geodynamic Evolution of East Antarctica (GEA)	2013-2015	(Eagles et al., 2021) https://doi.org/10.1594/PANGAEA.938357
Alfred Wegener Institute (AWI)	Oldest Ice Reconnaissance (OIR)	2016-2017	(Eisen et al., 2020) https://doi.pangaea.de/10.1594/PANGAEA.920619
British Antarctic Survey	Bedmap2; Soviet Antarctic Expedition (SAE) measurements	1964	(Fretwell et al., 2013): grid https://secure.antarctica.ac.uk/data/bedmap2/ (Kapitsa, 1964): data points
Centre for Remote Sensing of Ice Sheets (CReSIS), University of Kansas	RDS 2018 Antarctica Ground	2018-2019	(Rodriguez-Morales et al., 2020) https://ops.cresis.ku.edu/
NASA	Bedmachine	-	(Morlighem et al., 2020) https://nsidc.org/data/nsidc-0756/versions/3
National Institute of Polar Research (NIPR)	Japanese Antarctic Research Expedition (JARE) 33	1992-1993	(Tsutaki et al., 2021a) https://doi.org/10.17592/001.2021110902
	JARE 37	1996-1997	(Tsutaki et al., 2021b) https://doi.org/10.17592/001.2021110903
	JARE 40	1999-2000	(Tsutaki et al., 2021c) https://doi.org/10.17592/001.2021110904
	JARE 49	2007-2008	(Tsutaki et al., 2021d) 179 MHz: https://doi.org/10.17592/001.2021110905 (Tsutaki et al., 2021e) 60 MHz: https://doi.org/10.17592/001.2021110906
	JARE 54	2012-2013	(Tsutaki et al., 2021f) https://doi.org/10.17592/001.2021110907
	JARE 59	2017-2018	(Tsutaki et al., 2021g) https://doi.org/10.17592/001.2021110908 (Tsutaki et al., 2021h) https://doi.org/10.17592/001.2021110909
	JARE 60	2018-2019	(Tsutaki et al., 2021i) https://doi.org/10.17592/001.2021110910

S1.2 Calibration and standardization of ice-thickness measurements

Ice-thickness measurements were compiled from various sources (Table S1) and standardized if required. The two-way travel time (TWT) for transmitted radio wave reflections from the ice-surface minus the ice bottom were converted to ice-thickness (h) using:

$$h = \frac{TWT * V_{ice}}{2}$$

where V_{ice} is the propagation speed of radar waves in ice. To standardize these data from different sources we used a single $V_{ice} = 1.69 \times 10^8 \text{ m s}^{-1}$ which was used by Tsutaki et al. (2022) taking into account the ice properties observed in the Dome Fuji ice core. Applying this parameterization across all radar datasets also gives ice thicknesses within 500 m of the drilling site (Table S2) that are close to the estimate of $3028 \pm 15 \text{ m}$ at the core site (Fujita et al., 2006).

Table S2: Ice-thicknesses within 500 m of the DF1 core site.

Survey	Data Points	Mean (m)	Median (m)	STD (m)
AWI	56	3033.5	3036.2	11.2
CRISIS	51	3013.3	3013.0	14.7
JARE59	474	3017.0	3015.0	15.7
JARE49	1	3036.0	3036.0	-
All surveys	582	3018.3	3017.0	16.1

AWI: A firm correction of +10 m was removed from the OIR and GEA ice-thickness data and TWT was calculated from ice-thicknesses using the wave propagation speed of 1.67×10^8 used by Karlsson et al., (2018). We then used a wave propagation speed of $1.69 \times 10^8 \text{ m s}^{-1}$ to standardise ice-thickness estimates.

CRISIS: We calibrated for observed time 0 variability along each CRISIS survey line by tracking TWT for the first peak in returned power within the upper $0.7 \mu\text{s}$ and applying a gaussian smoothing function in a horizontal moving window of 500 data points (Figures S1, S2). The vertical search window was chosen after manual inspection of each survey line showed the first peak within the upper $0.7 \mu\text{s}$, which we assumed to be the ice surface. The TWT to ice bottom (i.e., ice-bed interface) was picked using semi-automated algorithms on newly processed echograms. Radar echograms were manually inspected, and layer picks adjusted using manual control points where necessary using the CRISIS Toolbox ("CRISIS Toolbox," 2021) working on MATLAB. The ice bottom TWT was subtracted from ice surface TWT to give ice thickness. TWT was converted to depth in meters using a wave propagation speed of $1.69 \times 10^8 \text{ m s}^{-1}$.

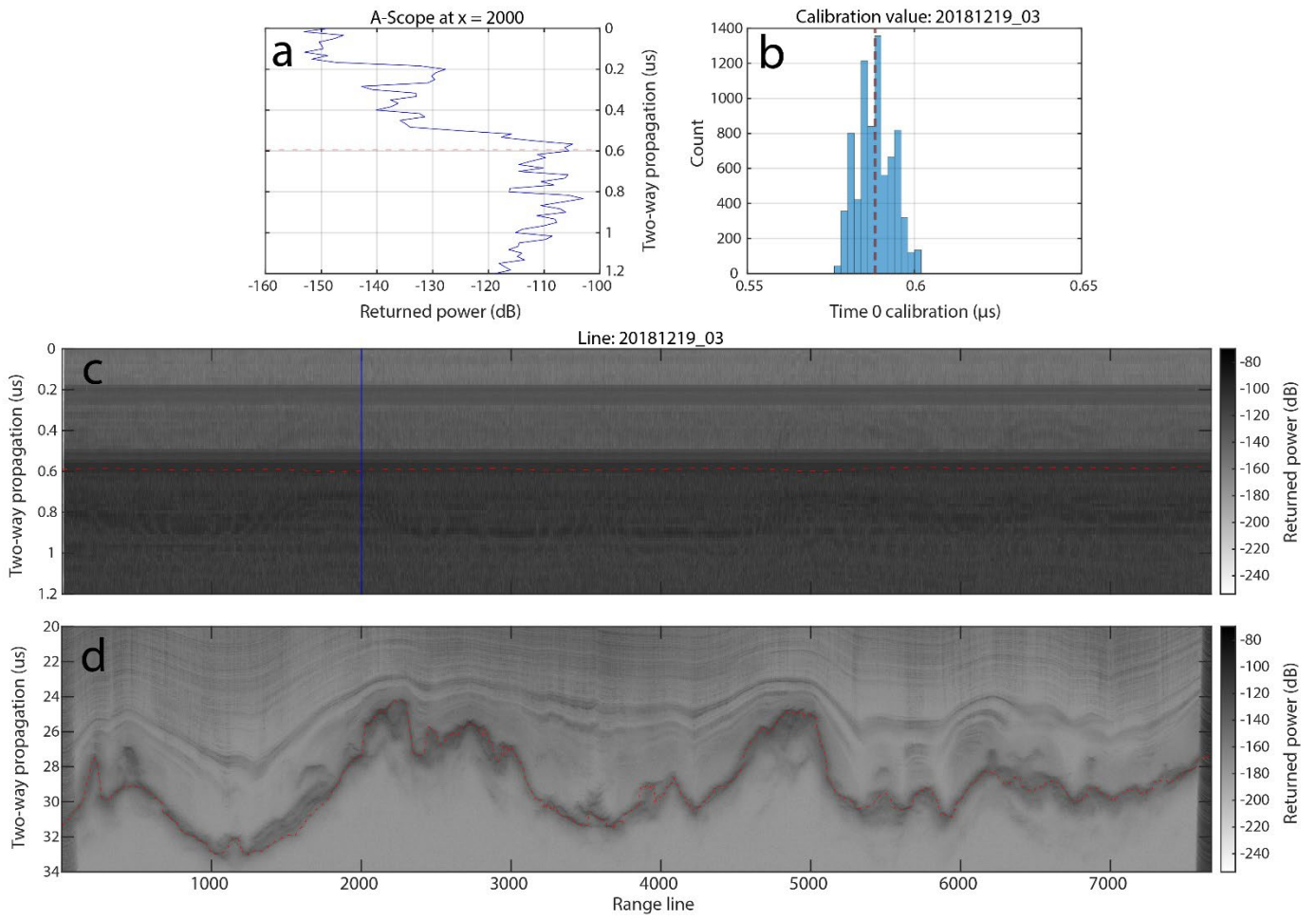


Figure S1: Time 0 calibration results for CReSIS ice-thickness data, for profile 20181219_03. **a)** Returned power (dB) plotted against TWT (μs) at position $x = 2000$ (blue line) on the echogram. TWT for the first peak is drawn in red. **b)** Distribution of TWTs to the first peak along this profile. Vertical red dashed line shows mean value. **c - d)** Echograms showing the ice surface reflection at 0 – 1.2 μs , and the bed reflection at 20 – 34 μs . The red line in panel **c** shows the calibrated ice sheet surface and the red curves in panel **d** show the picked bed reflector.

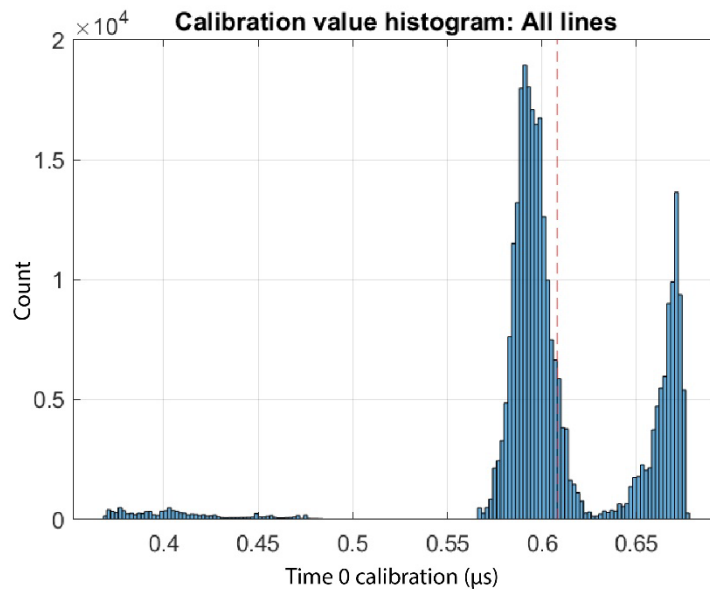


Figure S2: Distribution for all Time 0 calibration results for all CReSIS radar profiles and the mean value (red line).

S1.3 Crossover analysis

A crossover analysis was conducted between the CReSIS radar survey and three other radar surveys (JARE59, JARE60, and AWI OIR). AWI GEA data have no crossover points with CReSIS data. Measurements close to the survey basecamp with unstructured survey profiles were masked out in a 6 x 3 km region centred at 844125 Easting, 1037460 Northing. The XY locations of survey track crossover points was calculated, then a 30 m buffer was used to extract ice-thickness measurements and calculate mean values per survey. The crossover differences were calculated as CReSIS ice-thickness measurements minus JARE59, JARE60, AWI OIR measurements (Figure S3a), yielding respective median differences of 3 m, 18 m, and -1 m. The spatial distribution of differences (Figure S3b) does not show clustering of anomalously large or small differences and the median biases we observed were quite close to zero, so we chose not to calibrate the data further.

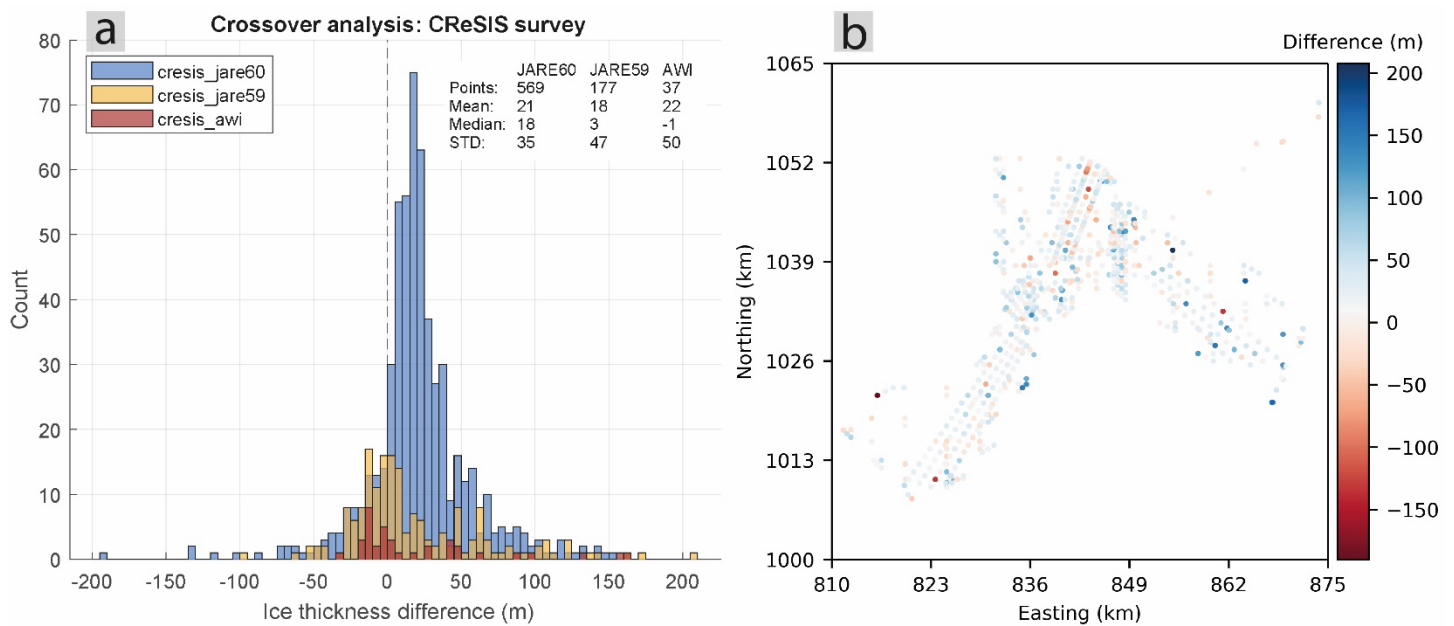


Figure S3: Crossover analysis. **a)** The distribution of ice-thickness measurement differences between the CReSIS radar survey and the AWI OIR, JARE 59, and JARE 60 surveys. **b)** Spatial distribution of survey measurement differences.

Text S2. Stochastic simulation of bed topography

S2.1 Software and tools

We used Python 3.9.7 to conduct the analysis, with packages for data manipulation, raster processing and analysis (numpy, rasterio, pandas, rioarray, rasterstats, xarray, pyproj, cartopy, scipy). We also used and adapted tools for geospatial/ geostatistical analysis and stochastic methods from the following open-source python packages: Verde (Uieda, 2018), GeoStatsPy (Pyrz et al., 2021), SciKit GStat (Mälicke et al., 2021), and GStatSim (Mackie et al., 2022). Specifically, the Verde 'BlockReduce' function was used for data decimation with median filter. From GeoStatsPy, the 'nscore' function was used to compute normal scores for ice-thickness data, 'gamv' function was used to compute experimental semivariograms, and 'vmodel' used to create exponential variogram models. From the GlacierStats package (Mackie et al., 2022) we used the 'okrige_sgs' function for sequential gaussian simulation algorithms based on ordinary kriging and several other tools during preliminary data analysis and experiments.

S2.2 Geostatistical model development and implementation

Decimated ice-thickness data were normalized using a normal score transformation so that the values fit a standard Gaussian distribution (Deutsch & Journel, 1997). Weighting parameters were stored to later transform values back into ice-thickness. Experimental semivariograms for ice-thickness data were calculated to find expected variance between data points as a function of distance. In preliminary experiments semivariograms were obtained for 4 azimuthal ranges of 45 degrees with centres at 0, 45, 90, and 135 degrees. We did not observe significant anisotropy in ice-thickness measurements (Figure S4a). We also simulated ice-thickness using regional semivariograms and models for up to 5 regions (Figure S4b) within the study area shown in Figure 1. Despite some difference between the central region (DF4 labelled in Figure S4b) and surrounding regions (DF0, DF1, DF2, DF3 and DF4) we found after fitting an exponential model that parameters were not different enough with this procedure to justify the extra time taken to run the analysis with region-specific statistical models. We therefore proceeded using an isotropic semivariogram, accepting a slight bias towards regionally higher roughness which we find appropriate given the ensemble-analysis approach. Based on the distance between survey profiles (0.5 – 15 km), maximum distance between ice-thickness data (15 km) and the scale of major topographic features (10's of km) we calculated an isotropic experimental semivariogram with maximum lag of 80 km at lag intervals of 500 m (Figure S5).

An exponential statistical model was fit to the experimental semivariogram using a Trust Region Reflection least squares function, with resulting range = 80000, sill = 1, nugget = 0 (Figure S5), representing the variance between ice-thickness measurements as a function of distance. The statistical model was used in SGS to estimate local mean and variance for a Gaussian probability density function at un-surveyed locations using ordinary kriging. A value is selected at random from this distribution to simulate the ice-thickness, and the grid cell is added to conditioning data and included in subsequent calculations. In initial experiments we examined the algorithm run time for different influencing factors, including number of conditioning data points for the probability distribution, the search radius around un-surveyed grid cells for conditioning data, the output grid cell size (between 0.1 and 5 km), the study region boundary, and the level of data decimation. We chose parameters of 40 nearby data points within a search radius of 30 km for our optimum experiment, yielding simulated topography with 500 m grid cells that kept the algorithm run times to an acceptable level.

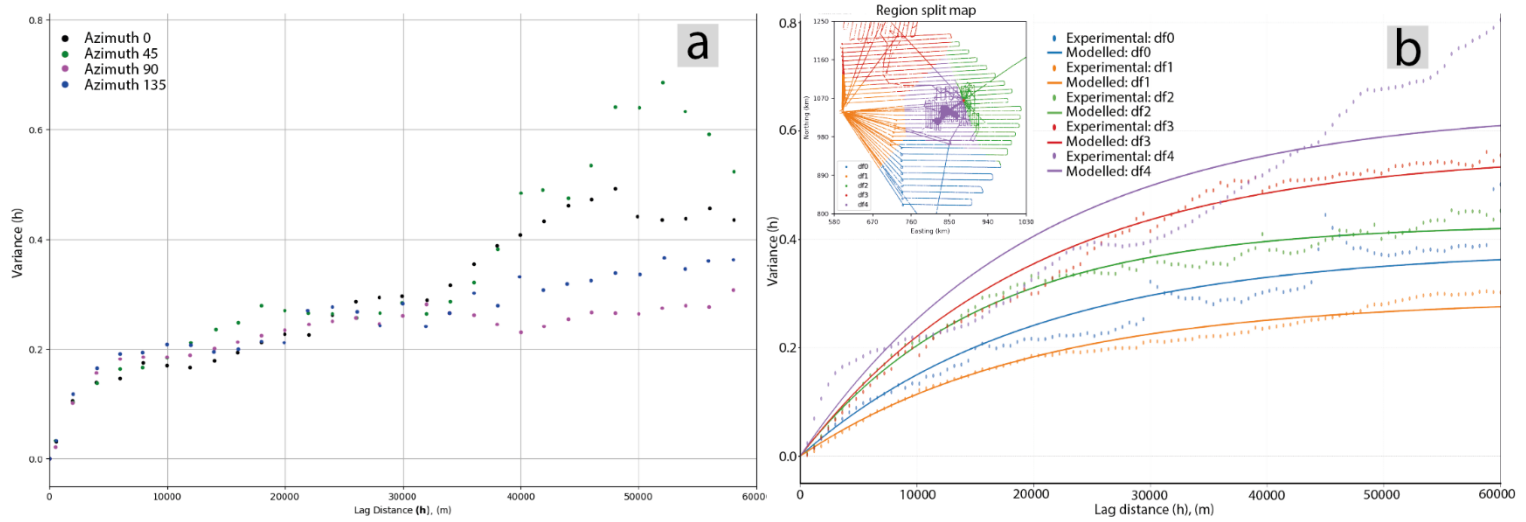


Figure S4: Experimental semivariograms and variogram models. **a)** Variograms across 4 azimuthal ranges for lag distance intervals of 2 km. Differences in variance are larger for lag distances over 40 km, but similar variance is observed for the different azimuths when the lag distance is less than 30 km which is the target range of this study. **b)** Regionally calculated experimental semivariograms and statistical models.

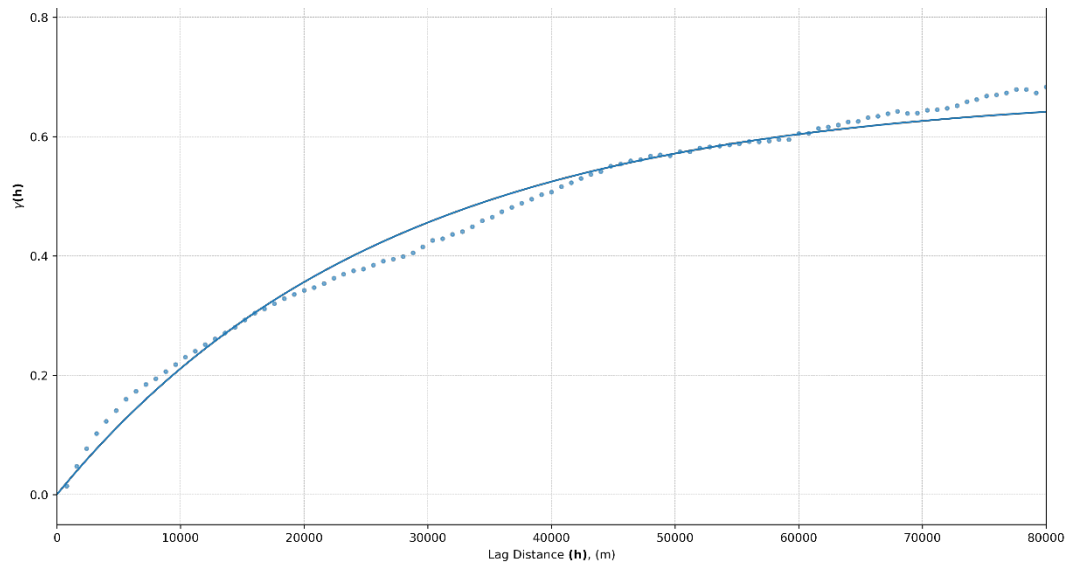


Figure S5: Optimum experiment exponential model (blue line) fit to the experimental semivariogram for ice-thickness data (blue dots).

Text S3. Results

All 100 simulated bed-topography, ice-thickness, and topographic geothermal heat flow adjustment grids are available at the Norwegian Polar Data Centre (<https://doi.org/10.21334/npolar.2023.dbd63194>). The results are in raster format (.tiff) in an Antarctic Polar Stereographic (EPSG: 3031) coordinate system. The spatial extent is 596000 m to 1020000 m Easting and 816000 m to 1240000 m Northing with cell size 500 m x 500 m (848 columns, 848 rows). Ice-thicknesses are provided in meters and bed elevations are in meters referenced to the WGS84 Ellipsoid.

S3.1 Validation of simulated bed

Over the entire study region (719,104 cells), 6.4% of the grid (46,374 cells) contain ice-thickness measurements and 94% (43,600 cells) of these contain 30 or fewer measurements. Figure S6a shows the number of ice-thickness measurements per grid cell for $1 \leq n \leq 30$. The bias at around 15 measurements per grid cell is likely sourced from the sample rates along radar profiles which are 15 - 30 m for CReSIS, JARE60 and AWI OIR data. Every simulated ice-thickness grid in our ensemble was assessed for agreement with the full ice-thickness measurements dataset (i.e., measurement data before decimation). Figure S7 shows the distributions for these differences and correlation between measurement data and simulated ice-thickness grid value at the measurement location. The mismatches have a large standard deviation ($\sigma = 51$ m), although this is within the expected range considering the measurement variability observed within each grid cell (Figure S6b).

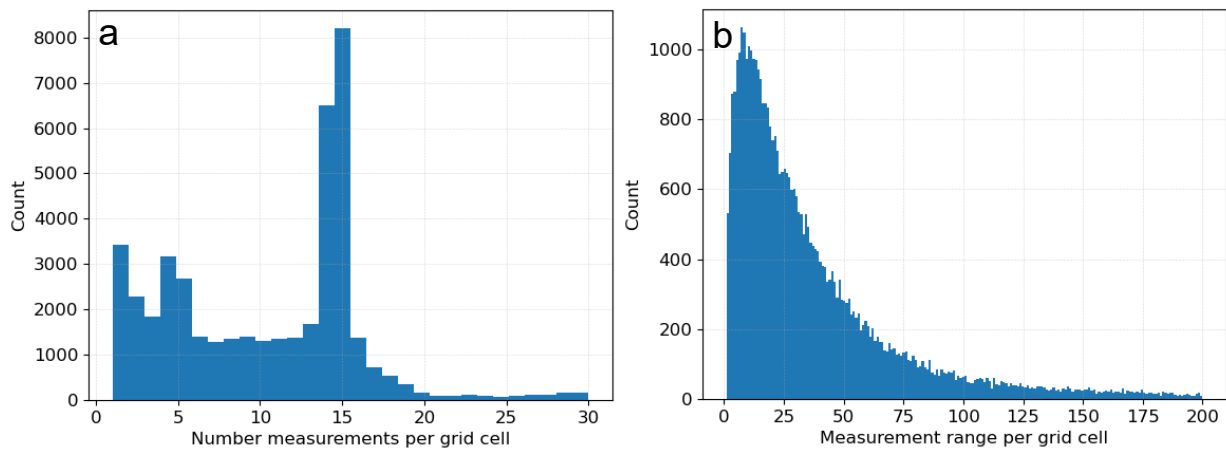


Figure S6: Statistics for ice-thickness measurements contained within each 500 m x 500 m cell of our results grid. **a)** Number of measurements per grid cell. **b)** The difference between the highest and lowest measurement per grid cell.

Bed roughness and topographic features are most reliable in regions with high measurement density and small distances between survey tracks. In regions with large spacings between survey lines, GHF adjustments cannot accurately reflect impacts at the scale of individual topographic features. However, regional spatial patterns of modification are realistic due to the consistency between interpolated values and measured local roughness characteristics. Beyond radar survey extents, for example outside AWI survey tracks (Figure 1a), the regional pattern and roughness characteristics of simulated subglacial topography reflect only the properties

of the BedMachine sample points. However, regularly-spaced 2 km sample points ensured little deviation from the streamline diffusion interpolations from Morlighem et al., (2020) and provided data in peripheral regions necessary to generate a contiguous grid.

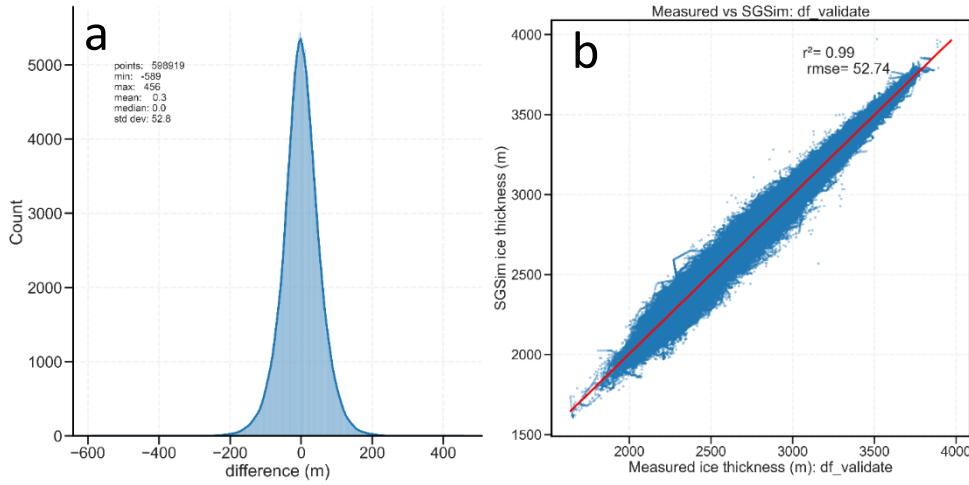


Figure S7: Validation results for SGS result #001. a) Measured minus simulated difference distribution. b) measured ice-thickness plotted against simulated grid cell value.

S3.2 Geothermal heat flow models and topographic adjustment

Figure S8 shows GHF in the Dome Fuji region for 7 different GHF models (Shen et al., 2020; Stål et al., 2020; An et al., 2015; Purucker, 2012; Losning et al., 2021; Martos et al., 2017; Burton-Johnson et al., 2020). Their distributions at native resolution are plotted in Figure 2d in the main text. The local GHF after topographic modification (G') was calculated following Colgan et al. (2021):

$$G' = G \left(1 + \frac{\Delta G}{G} \right), \quad (S1)$$

where G = modelled large-scale GHF estimate. $\Delta G/G$ = GHF perturbation by an anomaly, which is the function calculated by equation 1 in the main text (Section 2.3).

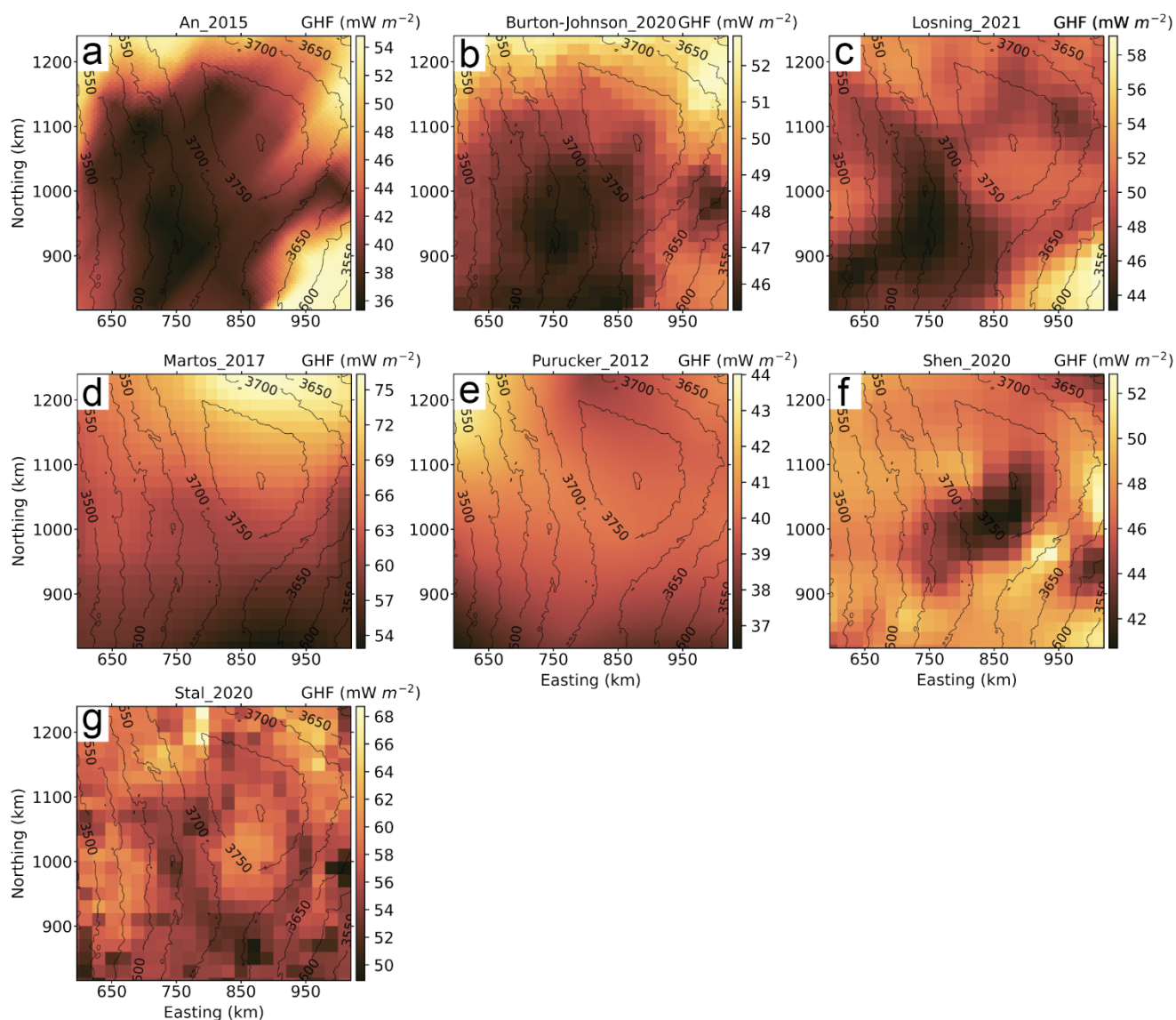


Figure S8: Modelled pan-Antarctic GHF sampled in the Dome Fuji region **a-g)** GHF maps labelled with associated publication (Shen et al., 2020; Stål et al., 2020; An et al., 2015; Purucker, 2012; Losning et al., 2021; Martos et al., 2017; Burton-Johnson et al., 2020). Ice surface contours drawn based on REMA (Howat et al., 2019). Note: different colour scale ranges due to wide spread of modelled GHF values.

S3.3 Bed roughness and uncertainty

Table S3: Statistics for linear regression models for Topographic Roughness Index (TRI) and Median Absolute Deviation (MAD).

Interval	Slope	Num. Obs.	RMSE	R ²
0-500	0.15875	85926	16.48698	0.329271
500-1000	0.25018	85004	14.96867	0.631985
1000-1500	0.32147	86489	14.13916	0.760733
1500-2000	0.37367	83717	14.28693	0.804909
2000-2500	0.41035	86320	14.77184	0.820207
2500-3000	0.44275	70812	16.08543	0.806945
3000-3500	0.47691	53239	17.27262	0.790263
3500-4000	0.50429	44616	17.98858	0.780341
4000-4500	0.52426	38351	18.36653	0.77619
4500-5000	0.53870	30809	18.77894	0.769702
5000-5500	0.57396	12751	17.51052	0.794966
5500-6000	0.58995	10759	17.36857	0.786223
6000-6500	0.60165	9543	17.17621	0.789962
6500-7000	0.61033	8328	16.71906	0.787735
7000-7500	0.61304	6229	16.33385	0.770303
7500-8000	0.64085	749	15.50713	0.720789
8000-8500	0.64211	420	14.53889	0.449234
8500-9000	0.65066	249	13.84399	0.30013
9000-9500	0.66853	89	12.28784	0.255493

Additional Supporting Information

Animated ensemble results are provided at

<https://doi.org/10.21334/npolar.2023.dbd63194> and have the following captions:

Movie S1: Simulated bed topography results ($n = 100$) as individual hillshaded relief maps animated at 3 frames per second. Ice surface contours drawn at 50 m intervals from Howat et al., (2019).

Movie S2: Topographic adjustments to background geothermal heat flow, based on simulated bed topography results ($n = 100$). Drawn as individual hillshaded relief maps and animated at 3 frames per second. Ice surface contours drawn at 50 m intervals from Howat et al., (2019).